



HAL
open science

Shape measurements of lattice materials from few X-ray radiographs using the 3D Virtual Image Correlation (3D-VIC) method

Lucie Calmettes, M.L.M. François, Julien Réthoré

► **To cite this version:**

Lucie Calmettes, M.L.M. François, Julien Réthoré. Shape measurements of lattice materials from few X-ray radiographs using the 3D Virtual Image Correlation (3D-VIC) method. *Experimental Mechanics*, inPress, 10.1007/s11340-024-01116-3 . hal-04362475v2

HAL Id: hal-04362475

<https://hal.science/hal-04362475v2>

Submitted on 24 Jul 2024

HAL is a multi-disciplinary open access archive for the deposit and dissemination of scientific research documents, whether they are published or not. The documents may come from teaching and research institutions in France or abroad, or from public or private research centers.

L'archive ouverte pluridisciplinaire **HAL**, est destinée au dépôt et à la diffusion de documents scientifiques de niveau recherche, publiés ou non, émanant des établissements d'enseignement et de recherche français ou étrangers, des laboratoires publics ou privés.



Distributed under a Creative Commons Attribution 4.0 International License

Shape measurements of lattice materials from few X-ray radiographs using the 3D Virtual Image Correlation (3D-VIC) method *

Lucie Calmettes^{1*}, Marc L.M. François^{1†} and Julien Réthoré^{1†}

^{1*}GeM, UMR 6183, Nantes Université, École Centrale Nantes, CNRS,
chemin de la Houssinière, Nantes, 44322, Pays de la Loire, France.

*Corresponding author(s). E-mail(s): lucie.calmettes@univ-nantes.fr;
Contributing authors: marc.francois@univ-nantes.fr;
julien.rethore@ec-nantes.fr;

†These authors contributed equally to this work.

Abstract

Background: the development of additive manufacturing technologies (3D printing) has made it possible to manufacture complex structures such as architected materials. However, traditional inspection methods are not suited to these materials, which require volume inspection to examine their internal structure.

Objective: the aim is to provide a 3D shape measurement method based on the initial computer-aided design (CAD) model used for 3D printing and X-ray radiographs.

Method: the CAD model is deformed until its virtual radiographs obtained by simulating the absorption of X-rays through the solid register with experimental radiographs. This registration is achieved by minimising a cost function with respect to the position of control points using radial basis function interpolation.

Results: the method's performance is first evaluated using synthetic data. Its robustness is assessed with respect to image resolution, number of radiographs and noise level. Subsequently, the geometry of a solid with a tetrahedral architecture was quantified by means of a mere five radiographs. Global variation in shape and local defects in lattice structure can be detected.

*License: CC-BY 4.0 @TheAuthors

Conclusions: the method enables the in-volume shape of architected materials to be checked without reconstructing the 3D computed tomography volume, but from just a few radiographs. It is robust and can detect local defects.

Keywords: VIC, 3D-VIC, CT-scan, architected materials, shape measurement

Introduction

The evolution of additive manufacturing technologies (3D printing) has enabled the creation of new complex structures, including architected materials. These materials offer a good compromise between mass and rigidity [1]. They can also be optimized for other applications, such as heat exchange [2, 3] or waveguiding and filtering [4, 5]. Architected materials possess an internal structure at some meso scale [6, 7] which is intermediate between the macroscopic scale of the whole structure, and the micro scale of the constitutive material. The macroscopic behavior of an architected material, for example homogenized elasticity and limit stress states, is clearly related to its mesoscopic geometry [8]. Many choices are possible for the meso scale arrangement, which can be regular according to some symmetry group, random, or even quasi-symmetric [9], [10]. Furthermore, the cellular materials in which voids are separated by walls (foams, honeycombs, . . .) are generally distinguished from the lattice materials composed of beams (3D trusses). The French ANR project MoMap, within this study was carried out, focuses on regular lattice materials with tetrahedral unit cells because of their high rigidity and strength.

In order to measure the shape of an architected material after 3D printing, it is necessary to carry out checks from the mesoscopic to the macroscopic scale. Conventional post-fabrication inspection methods (gages, ultrasound, etc. . .) are suitable for classical bulk materials but are no longer applicable to architected materials [6]. For this reason, image-based inspection methods, such as the one presented hereafter, are under development [11, 12].

In the field of mechanical engineering, the DIC (Digital Image Correlation) method is now commonly used for non-destructive and contactless measurement of displacement and deformation fields. At first developed for two-dimensional in-plane displacement measurement with a single camera, the DIC has proven to have a sub-pixel accuracy [13, 14]. The stereo-DIC technique enables the measurement of the 3D displacement vector of non planar surfaces, with at least two cameras or a moving camera [15–17]. The recent PhDIC method gives rise to the same quantities [18] by building a textured digital twin object surface based on an optical modelling of the scene. However these methods remain limited to the measurement of observable surfaces, therefore are not suitable for the measurement of the internal shape of the meso-structure of a lattice material.

The virtual image correlation (VIC) method initially applies for 2D shape and contour measurements [19, 20]. It consists in finding the best local correlation between an image of the boundary of an object and a virtual image. The latter is based on a parametric curve and mimics the white to black gradient of the boundary. The curve equation acts as an optimal filtering and the correlation method is close to the one used in DIC. The precision of the shape measurement has been proven to be sub-pixel and noise resistant [21]. It takes advantage of the knowledge of an ideal reference geometry and of a simple synthetic image generation model.

The internal structure can be revealed by computed X-Ray tomography (CT scan). It consists in a reconstruction of the 3D image from a collection of radiographs, possibly projections, of the object which are acquired at many angles of rotation. The first use was for medical imaging. Various algorithms have been developed for the reconstruction of the 3D images such as ancient Hough and Radon transforms. The more recent Filtered Back Projections (FPB) method, based on Fourier transforms is highly effective in the case where tomographic data have low noise, but it requires a large

number of projections. The Algebraic Reconstruction Methods (ART) which are iterative and thus require more computing time, offer better reconstruction quality and are often preferred nowadays. They are based on the minimization of the quadratic norm of the difference between the projections of the reconstructed volume and the projections acquired with the tomograph, while the initial volume can be reconstructed with an FPB method.

However, a CT scan is not straightforwardly adapted to metrology, in its sense of precise shape measurements of industrial parts. Firstly, a 3D image represents the boundaries in the form of a variation in grey levels, which requires additional analysis to measure the shape, such as thresholding (and filtering) or a VIC like those developed previously [12, 22]). As a consequence, the biases induced by the reconstruction algorithm are combined with those of this further analysis. Furthermore, in an industrial point of view, the thousands of required projections for volume reconstruction are expensive. This method shares with PhDIC that synthetic images obtained by mimicking the optical system are compared to actual ones in order to identify the sought differences from the digital model to the object. The objectives of medical imaging differ from the objectives of metrological measurements on architected materials. Medical imaging has to deal with biological objects of unknown shapes and densities, unlike engineering objects whose shape deviate little from their known design and whose matter is fairly homogeneous.

The first extension of the DIC method in 3D, the DVC (Digital Volume Correlation), uses such reconstructed 3D images [23, 24] and requires natural 3D speckle or texture. In order to avoid using huge 3D images, the P-DVC consists in computing the correlations on 2D projections [25, 26]. Only a small number of projections is needed to measure displacement after an initial state volume image has been reconstructed.

The VIC has also been developed in 3D for surface detection in a 3D image. Applications have included measuring biological organ boundaries [22], crack surfaces [27]

and architectural materials metrology using CAD models [12]. The principle is an extension of the 2D VIC: a virtual volume image is generated from a mathematical surface equation and correlated with the reconstructed 3D image. Recently, Fragnaud et al. [11] improved the method by generating a whole 3D virtual image (digital twin) taking into account diffusion and scattering effect which occur in dense materials such as metals, thus increasing the precision of the method. However, as already mentioned, these methods use the reconstructed 3D image, which is therefore dependent upon the precision of the reconstruction and requires a significant number of projections, thus necessitating a substantial amount of computing and experimental time. Following the idea of the P-DVC, we propose in this article the 3D-VIC method in which the projections are registered with digital twins (virtual projections) based on an adjustable CAD model (using shape parameters) of the object.

Section 1 details the construction of the virtual projections from simulated X-rays propagation and the CAD model, taking into account the whole geometry of the tomograph. We take into account the absorption of X-rays by the material according to the Beer-Lambert law. We chose not to model diffusion and scattering effects which are not important for the polymeric materials and out of focus of this preliminary study. The rasterisation process, used to compute the distance travelled by a virtual X-ray through the 3D model, is also detailed. Section 2 shows the retained cost function which is basically the mean over the projection images and for the considered projection angles of squared differences from virtual and physical projections. Section 3 details the identification of the local motion modifying the shape of the CAD model. Using a CAD description, one may think that these local displacements could be identified by searching the displacement of each mesh node describing the CAD. However, a mesh node position interpolation method is preferred. Among those available, the Radial Basis Function (RBF) method was chosen as it allows smooth, local deformation [28]. For assessing the robustness of the proposed method, Section 4 analyzes

the algorithm's performance on synthetically generated projections. Firstly the effect of the method parameters (number of projections and supersampling) on the shape measurement are discussed. Secondly, the effect of image noise on accuracy is tested. The last Section 5 presents the analysis of real projections of a 3D tetrahedral lattice material printed by polymer wire deposition. Unsurprisingly, the measured shape differs significantly from the initial CAD model. Since no other method is available to compare with, we analyze the consistency of the identified shape defects from the knowledge of the printing process.

1 Virtual projections

The method consists in the registration of virtual and real projections. We model the X-ray tomograph and the specimen as (Figure 1):

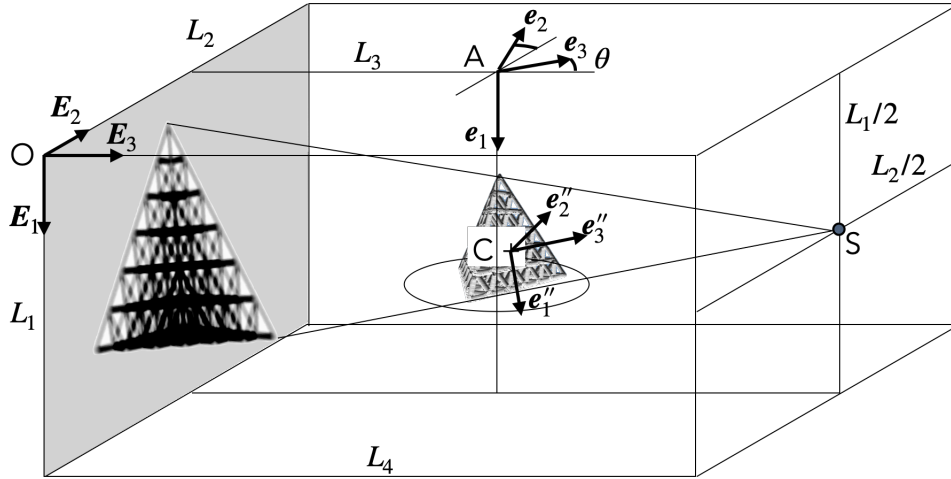


Fig. 1: tomograph model

- the tomograph reference frame $(O, \mathbf{E}_1, \mathbf{E}_2, \mathbf{E}_3)$ where $(O, \mathbf{E}_1, \mathbf{E}_2)$ is associated to the detector plane
- the rotating plate frame $(A, \mathbf{e}_1, \mathbf{e}_2, \mathbf{e}_3)$ where (A, \mathbf{e}_1) is its rotation axis. In this study we suppose that this device has no misalignment thus $\mathbf{e}_1 = \mathbf{E}_1$
- the rotating plate angle θ is measured from \mathbf{E}_2 to \mathbf{e}_2 . It is imposed by the rotating stage and we shall suppose this value to be known and exact
- the X-ray source point S whose perpendicular projection corresponds to the center of the detector.

For any point, the link between its coordinates (x, y, z) in the rotating stage frame $(A, \mathbf{e}_1, \mathbf{e}_2, \mathbf{e}_3)$ and (X, Y, Z) in the reference frame $(O, \mathbf{E}_1, \mathbf{E}_2, \mathbf{E}_3)$ is given by:

$$\begin{bmatrix} X \\ Y \\ Z \end{bmatrix} = \begin{bmatrix} 1 & 0 & 0 \\ 0 & \cos \theta & -\sin \theta \\ 0 & \sin \theta & \cos \theta \end{bmatrix} \begin{bmatrix} x \\ y \\ z \end{bmatrix} + \begin{bmatrix} X(A) \\ Y(A) \\ Z(A) \end{bmatrix}, \quad (1)$$

where $(X(A), Y(A), Z(A))$ are the coordinates of point A in the tomograph reference frame. Furthermore we define the lengths :

$$L_3 = Z(A), \quad (2)$$

$$L_4 = Z(S). \quad (3)$$

For any point, the link between its coordinates (x'', y'', z'') in the object frame $(C, \mathbf{e}_1'', \mathbf{e}_2'', \mathbf{e}_3'')$ and (x, y, z) in the rotating stage frame $(A, \mathbf{e}_1, \mathbf{e}_2, \mathbf{e}_3)$ is given by a combination of three rotations:

$$\begin{bmatrix} x \\ y \\ z \end{bmatrix} = \begin{bmatrix} \cos \alpha & 0 & \sin \alpha \\ 0 & 1 & 0 \\ -\sin \alpha & 0 & \cos \alpha \end{bmatrix} \begin{bmatrix} \cos \omega & -\sin \omega & 0 \\ \sin \omega & \cos \omega & 0 \\ 0 & 0 & 1 \end{bmatrix} \begin{bmatrix} 1 & 0 & 0 \\ 0 & \cos \beta & -\sin \beta \\ 0 & \sin \beta & \cos \beta \end{bmatrix} \begin{bmatrix} x'' \\ y'' \\ z'' \end{bmatrix} + \begin{bmatrix} x(C) \\ y(C) \\ z(C) \end{bmatrix}, \quad (4)$$

where (α, β, ω) are the Euler angles. For sake of clarity, these intermediate frames are not represented on Figure 1.

The X-ray intensities transmitted to the sensor are conditioned by the thickness of the traversed material *via* the Beer-Lambert law. This thickness is calculated from the CAD model using the rasterization method [29]. The ray tracing method could also be used. However, having no need for reflection computation, the rasterization method has been chosen for its numerical efficiency [30]. For any pixel center point M of the

detector, this method allows us to compute the traversed length $L(M)$ along the path SM , where S is the punctual X-ray source. This distance is calculated by summing the distances between the points at which the ray enters and exits the material.

In practice, the surface of the CAD model is discretized using a triangular mesh where the nodes are V_j with $j \in [1, \dots, N_f]$, N_f being the number of nodes.

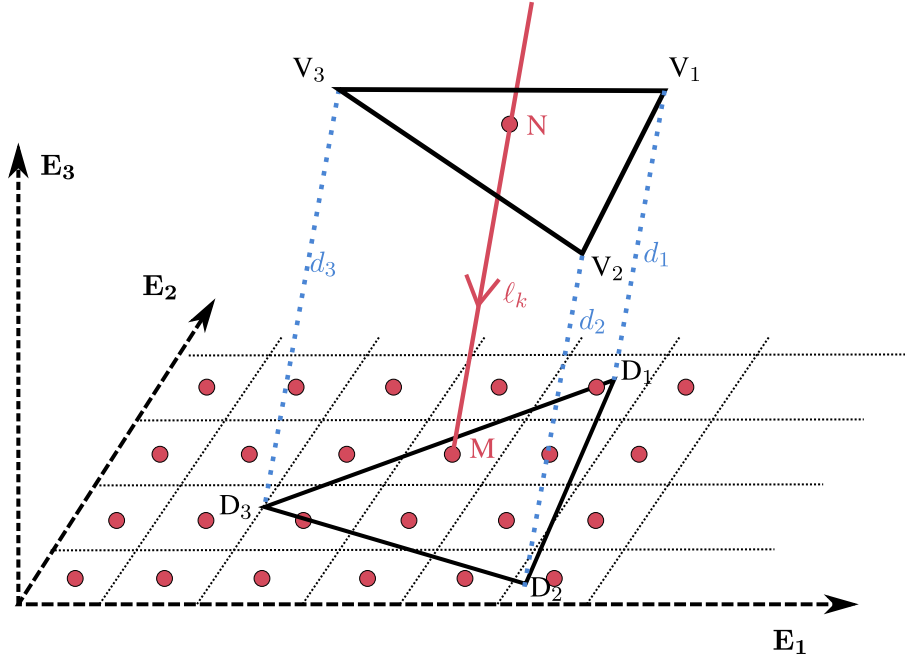


Fig. 2: Illustration of rasterization technique, projections (D_1, D_2, D_3) of the vertices of the triangle (V_1, V_2, V_3).

A triangle (V_1, V_2, V_3) intersects a ray SM if the projected triangle (D_1, D_2, D_3) onto the detector plane contains the pixel M (see Figure 2). The barycentric

coordinates (w_1, w_2, w_3) of M are:

$$\begin{aligned} w_1 &= \frac{a(D_3D_2M)}{a(D_1D_2D_3)} \\ w_2 &= \frac{a(D_1D_3M)}{a(D_1D_2D_3)}, \\ w_3 &= \frac{a(D_2D_1M)}{a(D_1D_2D_3)} \end{aligned} \quad (5)$$

where a stands for the area of the triangle. The position vector $\mathbf{X}(M)$ is then written as:

$$\mathbf{X}(M) = w_1\mathbf{X}(D_1) + w_2\mathbf{X}(D_2) + w_3\mathbf{X}(D_3), \quad (6)$$

where $\mathbf{X}(D_j)$, for $j = 1..3$, are the position vectors of D_1, D_2, D_3 . The beam passes by this triangle if $0 \leq w_1, w_2, w_3 \leq 1$ and $w_1 + w_2 + w_3 = 1$. The distance ℓ_k between the points M and N, where N is the intersection of the ray with the triangle (V_1, V_2, V_3) is [29, 31]:

$$\ell_k(M) = \sum_{i=1}^3 w_i d_i, \quad (7)$$

where d_i stands for the distance between points V_i and D_i . This distance $\ell_k(M)$, as well as that of other intersected triangles, is stored in a Z-buffer relatively to the pixel M. These distances are sorted in ascending order, so that the beam enters the material through triangles with an odd k index and exits the material through triangles with an even k index. The researched distance traveled within the matter $L(M)$ for this pixel is:

$$L(M) = \sum_{K=1}^{N_K/2} (\ell_{2K} - \ell_{2K-1}), \quad (8)$$

where N_K is the (even) number of intersected triangles. For any rotating angle θ of the rotating stage, the intensity received by the pixel is calculated using Beer-Lambert's

law:

$$I_\theta(M) = I_0 \exp(-\mu L(M)), \quad (9)$$

where I_0 is the blank intensity and μ the absorption coefficient, supposed homogenous.

The gray level of the virtual projection $G_\theta(M)$ at the pixel M is computed from $L(M)$ only:

$$G_\theta(M) = -\log \frac{I_\theta(M)}{I_0}, \quad (10)$$

$$= \mu L(M). \quad (11)$$

This virtual projection G_θ will be registered with the real projection.

During the physical imaging process, each pixel captures a significant number of X-rays. In contrast, when simulating this process for the construction of virtual projections, above method involves only one ray per pixel. To make virtual projections more realistic, they are computed over a B times finer pixel grid (B being the supersampling factor) and then binned (averaged) to match the resolution of physical images. This supersampling technique is commonly used in volumetric reconstruction methods from radiographs to reduce computation times by generating less noisy lower-resolution radiographs [32, 33].

2 Registration procedure

The cost function Ψ of the proposed 3D-VIC method allows one to evaluate the correlation between the n_θ virtual and real projections. The real projections F_θ are computed from the radiographs I_θ acquired by the tomograph using the white fields I_0 and following Equation (10). The virtual projections G_θ (see previous section) depend upon the tomograph parameters (points $\{S, A, C\}$ and angles (α, β, ω)) and upon the shape parameters λ_i which will be further specified in the next section. All the distances are expressed in meters. The cost function is defined from the average of the quadratic distance between the all the projections:

$$\Psi(\lambda_1, \dots, \lambda_n) = \frac{1}{n_\theta L_1 L_2} \sum_\theta \int_0^{L_1} \int_0^{L_2} (F_\theta - G_\theta)^2 dX dY, \quad (12)$$

where (L_1, L_2) are the lengths of the detector plane, respectively along $\mathbf{E}_1, \mathbf{E}_2$. This simple expression is commonly used in DIC for its simplicity and numerical efficiency [34, 35]. The measured tomograph and shape parameters are defined as the ones which minimize the cost function Ψ .

The minimization of Ψ is achieved thanks to a Newton scheme:

$$\lambda_i^{k+1} = \lambda_i^k - \left[\frac{\partial^2 \Psi^k}{\partial \lambda_i \partial \lambda_j} \right]^{-1} \frac{\partial \Psi^k}{\partial \lambda_j}, \quad (13)$$

where k is the number of the current iteration and where:

$$\frac{\partial \Psi}{\partial \lambda_i} = \frac{1}{n_\theta L_1 L_2} \sum_\theta \int_0^{L_1} \int_0^{L_2} -2(F_\theta - G_\theta) \frac{\partial G_\theta}{\partial \lambda_i} dX dY, \quad (14)$$

$$\frac{\partial^2 \Psi}{\partial \lambda_i \partial \lambda_j} = \frac{1}{n_\theta L_1 L_2} \sum_\theta \int_0^{L_1} \int_0^{L_2} 2 \left(-(F_\theta - G_\theta) \frac{\partial^2 G_\theta}{\partial \lambda_i \partial \lambda_j} + \frac{\partial G_\theta}{\partial \lambda_i} \frac{\partial G_\theta}{\partial \lambda_j} \right) dX dY. \quad (15)$$

As in VIC [19] and DIC [36] theories, it is assumed that, as the cost function goes to zero, the term involving the second derivative of G_θ can be neglected. Thus we retain:

$$\frac{\partial \Psi^2}{\partial \lambda_i \partial \lambda_j} \simeq \frac{1}{n_\theta L_1 L_2} \sum_\theta \int_0^{L_1} \int_0^{L_2} 2 \left(\frac{\partial G_\theta}{\partial \lambda_i} \frac{\partial G_\theta}{\partial \lambda_j} \right) dX dY. \quad (16)$$

The derivatives of G_θ are computed from a right numerical differentiation. The algorithm stopping criteria are one in convergence speed and one in the relative value of the corrector $\|\lambda_j^k - \lambda_j^{k-1}\| / \|\lambda_j^k\|$.

3 Local shape corrections using Radial Basis Functions

For the registration matrix to be sparse, each shape parameter must have a local action on the CAD model shape. However, moving each node V_j of the CAD mesh would result in too local modifications and in many shape parameters. Further, conditioning problems can be encountered when a tangential motion of a node does not change the shape of the model. A less local action, consistent with the precision of tomography and VIC, is obtained by using Radial Basis Functions (RBF) [28, 37].

The RBF scheme interpolation is defined by the displacement vector $\boldsymbol{\gamma}_i$ of the \mathcal{N}_C control points C_i which infer the displacement vector $\mathbf{u}(V_j)$ of surrounding mesh nodes V_j thanks to a Gaussian weighting φ :

$$\mathbf{u}(V_j) = \sum_{i=1}^{\mathcal{N}_c} \boldsymbol{\gamma}_i \varphi(C_i, V_j), \quad (17)$$

$$\varphi(C_i, V_j) = \exp\left(-\left(\frac{\|\mathbf{x}(V_j) - \mathbf{x}(C_i)\|}{r}\right)^2\right), \quad (18)$$

where $r > 0$ is the RBF dimensional parameter.

Note that, in general, the displacement of the a node V_j at the same position as a control point C_i does not have the same displacement: $\mathbf{u}(V_j = C_i) \neq \boldsymbol{\gamma}_i$. The RBF method is renowned for its interpolation quality [38]. The value of the RBF dimensional parameter r significantly affects the stability and the accuracy of the interpolation process. The larger r , the larger the influence volume of each control points, thus a smoother deformation of the CAD mesh, but the denser the matrix in Equation 16. In practice, r is chosen such as the supports of the Gaussian functions overlap significantly *i.e.* when $r > 0.5h$, where h is the length between the RBF control points.

The RBF method is implemented in the Python programming language using the PyGeM library, which includes various morphing methods for mesh deformation [39]. The 3D-VIC shape parameters λ_j are the $3 \times \mathcal{N}_C$ components of the RBF control points displacements γ_i .

4 Performance analysis on synthetic radiographs

The precision of the proposed 3D-VIC method is tested on synthetic data sets. To this aim, a set of synthetic projections is generated from a reference CAD model (Figure 3) and is considered as experimental data. In the first test in Section 4.1, we study the influence of the major settings of the method which are the number of projections and the supersampling factor used to compute the virtual projections. In the second test in Section 4.2, we study the influence of image noise.

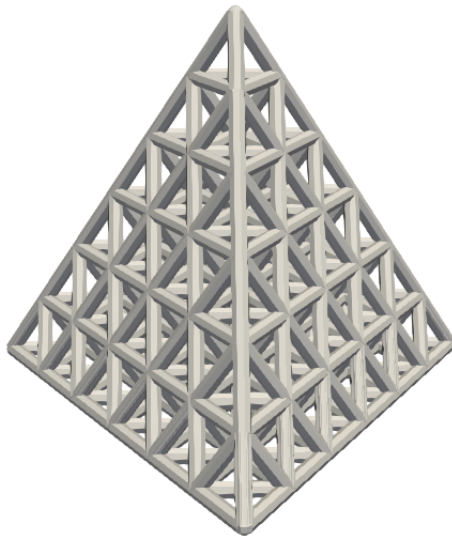


Fig. 3: CAD model of the tetrahedral lattice material

The MoMaP project, of which this research is a part, deals with regular lattice materials with tetrahedral unit cells. Consequently, the test is performed on a regular assembly of tetrahedral cells, forming a tetrahedron with 6 cells along on each side (Figure 3), thus 56 cells in the volume. This is enough to deal with hidden faces and fairly large Z-buffers but remains small enough that the projections, even with some noise, still contain the information about the inner shapes. The projections have a resolution of 235×187 pixels (Figure 6).

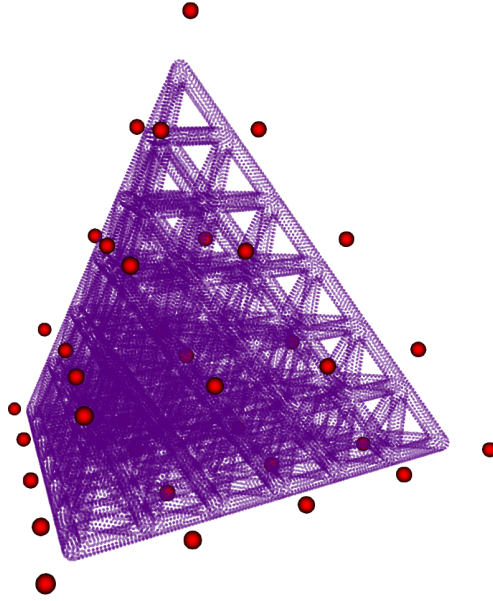


Fig. 4: Reference part and the 35 RBF control points at their original location (red)

The 3D-VIC measurement is performed with a deformable CAD model, parameterized by 35 uniformly distributed RBF control points (Figure 4). As a consequence, the set of the shape parameters in λ_j are the 3×35 components of the RBF control point displacements. In this section, the number of iterations is limited to 10.

The synthetic projections being obtained with the original CAD model, a measurement is exact if all the control points have a zero displacement at the end of the computation. Due to the limited number of projections, due to the use of a lower supersampling (see Section 4.1) factor for virtual projections than for synthetic projections or due to sensor noise (see Section 4.2), the measure is not exact and the RBF control points move from their initial position. The measurement error is defined as the standard deviation of the Euclidean norm of the displacement $\mathbf{u}(C_i)$ of the RBF

control points, from their initial (and expected) position:

$$\Delta = \sqrt{\sum_{i=1}^{\mathcal{N}_C} \frac{\|\mathbf{u}(C_i)\|^2}{3\mathcal{N}_C p^2}}, \quad (19)$$

where p is the detector pixel size (m/pix).

4.1 Influence of supersampling and number of projections

In order to represent flawless data, while maintaining a reasonable calculation time, the synthetic projections have been generated with a supersampling factor of $B_0 = 10$. From Section 1, this means that the gray level of each pixel is computed as the average over the value of 100 subpixels computed from 100 corresponding rays. The influence of the supersampling factor for virtual projections is tested by varying it from $B = 1$ to $B = 4$. Of course, the value $B = B_0 = 10$ has also been tested but is meaningless except to check that it actually gives a zero distance to the exact shape. The influence of the number of projections is tested from $n_\theta = 2$ to $n_\theta = 8$. The angle θ between two successive projections is constant at π/n_θ .

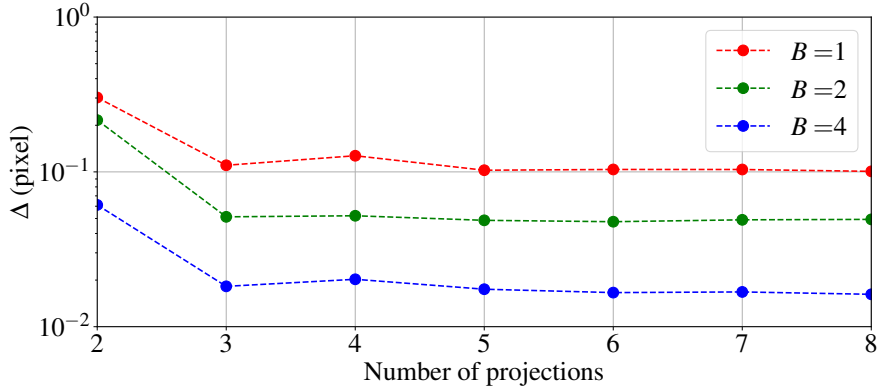
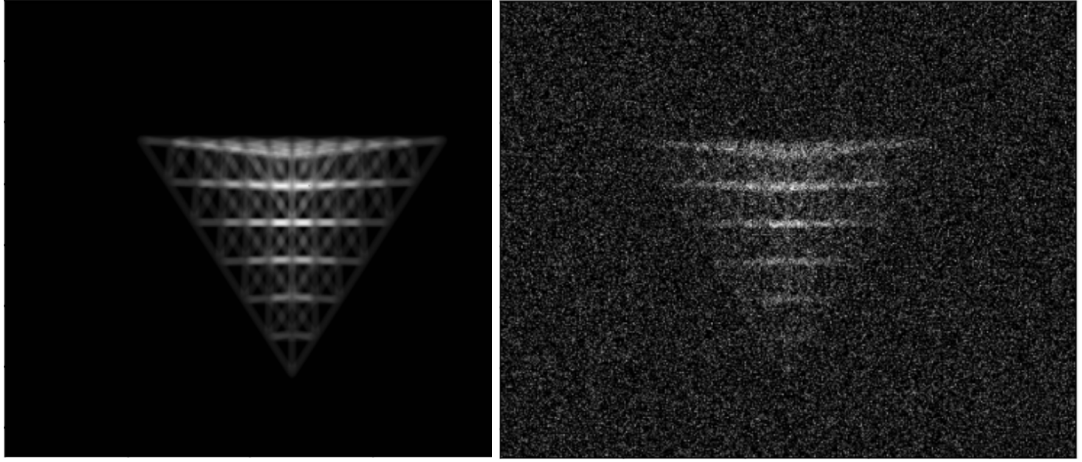


Fig. 5: Measurement error Δ as a function of the number of projections for different supersampling factor B .

As shown by Figure 5, the error of measure is already sub-pixel for two projections and $B = 1$ (no supersampling). For a supersampling of 4 and at least 3 projections, the error is less than 2×10^{-2} pixel. The gain is little beyond 5 projections, a value which is much lower than the thousands of projections required by conventional X-ray tomography reconstruction methods. This observation on the low number of required projections for projection-based methods is also made in other contexts, by other authors [11, 26]. Note that the somewhat singular value for 3 projections corresponds to the $2\pi/3$ rotation invariance of the tetrahedral lattice. Figure 5 shows also that the higher the supersampling factor the better the precision. Values for $B > 4$ are not representative because too close to the value of $B = 10$ used for synthetic projections. The computational cost depends quadratically on B whereas it depends only linearly upon the number of projections. As a conclusion, the performance comes with high supersampling factors with a quadratically increasing computational cost. Even for a very moderate supersampling $B = 2$ and a reduced number of projections, the 3D-VIC measurement has clearly a sub-pixel precision in this noiseless case.

4.2 Influence of sensor noise

The second test concerns the effect of image noise. For this purpose, the synthetic projections F_θ used in the previous test as physical images are, after rescaling, added with a Gaussian image noise H_θ of variance σ^2 and zero-mean. Its dependence on θ means that it is also temporally (from one projection angle to the next one) uncorrelated. Such spatially and temporally uncorrelated noise mimics the noise of the imaging system, of various physical origins including quantum, thermal and quantization noises. Out-of-limits values are clipped. When σ ranges from 0 to 0.25, knowing that 95% of the obtained values are in $[-2\sigma, 2\sigma]$ and that the grey values range from 0 to 1, this corresponds to a noise level of between 0 and 50% (see Figure 6).



(a)

(b)

Fig. 6: (a) Projection without noise, (b) Projection with $\sigma = 0.25$.

For this test, we used 4 projections, 35 control points and no supersampling ($B = 1$) for both physical (synthetic in this case) and virtual projections in order not to take into account the effect of the supersampling factor and to shorten the computation time. Figure 7 shows the results for some noise levels $\sigma \in [0, 0.25]$.

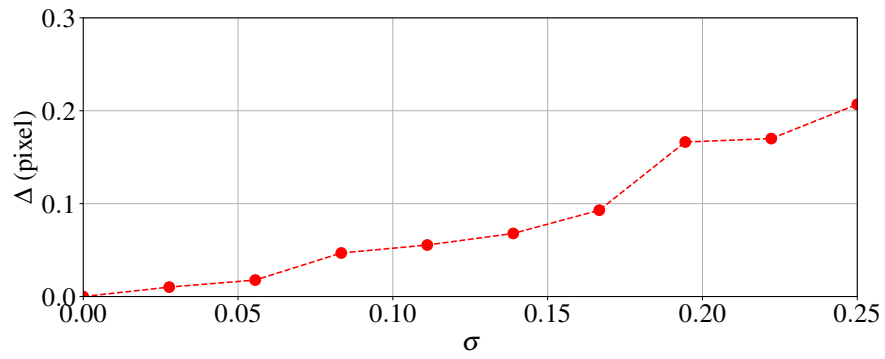


Fig. 7: Measurement error as a function of the noise level

It shows the increase of the error Δ with the noise amplitude. However, it is worth noting that even for a noise level going up to 50% the sub-pixel accuracy is preserved. This illustrates the ability of the proposed approach to measure the shape of a lattice even with a reduced amount of data (only a few projections) and its low noise sensitivity. This low sensitivity to uncorrelated noise is common for VIC methods [21]. It is due to the filtering effect, brought here by the use of RBF functions whose support, with $r = 0.85 h$, is larger than the distance between control points.

5 An example of practical use

The tetrahedron lattice shown in Figure 3 has been wireframe printed in ABS with a Zortrax M200. The tomograph is a RX-Solutions Ultratom set to 100 kV, which belongs to the ISIS4D Platform at Université de Lille (France). The native resolution of the projections is 1496×1880 pixels. To save computing time and reduce noise [33], they were binned with $B = 8$ to a resolution of 187×235 . A set of 1441 images were taken per revolution.

At first we show in Figure 8 the classic CT-scan obtained from this imaging. It has been reconstructed thanks to classical FBP, then thresholded using the Fast Marching Cube method and meshed using the Trimesh Python library [40].

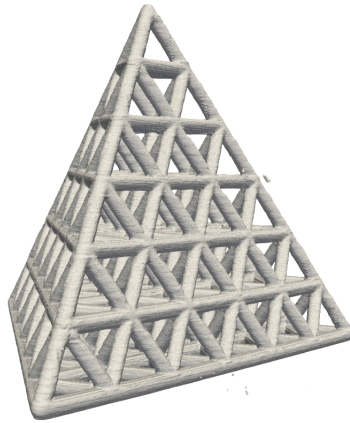


Fig. 8: 3D rendering of the reconstructed mesh obtained from the CT-scan of the studied specimen.

While unintended details such as print layers are clearly visible, shape defects are not because, in the absence of a reference shape, no shape defect, i.e. no comparison to this reference, is available. In addition, the rough surface makes filtering necessary before any measurement process, for example using previous VIC methods [12, 22]. As

mentioned above, using a CT scan involves three steps before measurement: 3D reconstruction, filtering and surface detection. In contrast, these three stages are carried out simultaneously using the proposed 3D-VIC method. Finally, the 3D-VIC measurement that follows was carried out using 5 projections instead of the 1441 used here.

Compared with the simulated measurement in the previous section, a real measurement requires a few extra steps. At first, the radiographs are converted into projections after being classically divided by the white fields. At second, an initial calibration of the tomograph configuration is carried out. To do so, the same optimization procedure as the one presented in the previous section is used but instead of adjusting the shape parameters, the sole parameters defining the virtual tomograph are adjusted. The source and the rotating stage will be supposed as perfectly aligned, so, in the global reference frame $(\mathbf{E}_1, \mathbf{E}_2, \mathbf{E}_3)$ the coordinates of S and A are $S(L_1/2, L_2/2, L_4)$ and $A(0, L_2/2, L_3)$ (see Figure 1). The remaining parameters to be adjusted are:

- the four lengths L_1, L_2, L_3 and L_4
- the three positioning angles α, β and ω
- the three coordinates of C
- the absorption coefficient μ

In this first calibration step in which the 11 parameters of the tomograph are adjusted (considered as the set λ_i of optimisation parameters of the cost function), the tetrahedral lattice obtained after 3D printing is considered to be sufficiently consistent with its CAD model. In other words, it is assumed that the geometrical defects of the object compared to its CAD model do not affect the evaluation of the tomograph model parameters and of the positioning of the object. This calibration is preceded from a manual setting of $(\alpha, \beta, \omega, x(C), y(C), z(C))$ and of the machine lengths L_i . Figure 9 shows the evolution of one of the virtual projections which becomes visually closer to the real one during this calibration step.

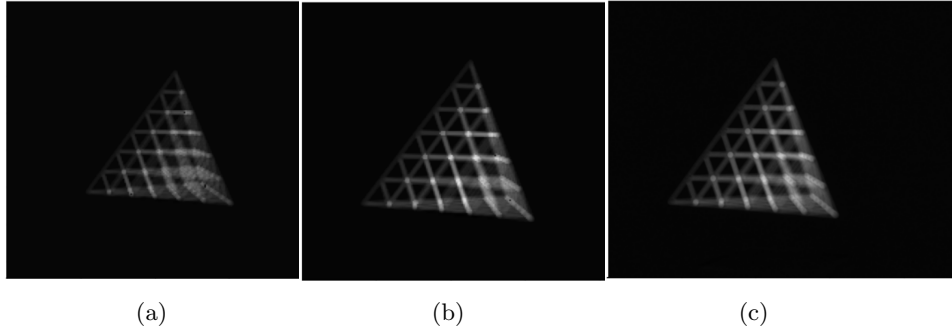


Fig. 9: Projections for $\theta = 0$: (a) virtual projection before calibration, (b) virtual projection after calibration and (c) corresponding real projection obtained with the tomograph.

Once the tomograph parameters and the position of the tetrahedral lattice have been obtained, the shape measurement can be performed. This time, the λ_i optimization parameters are the $3 \times \mathcal{N}_C$ components of the RBF control points displacements γ_i . The computations were performed considering only 5 projections (21° , 63° , 84° , 105° and 126°), using a supersampling ratio for the virtual projections of $B = 4$ and a maximum of 6 iterations. Two successive steps are shown which differ from the number and the location of the control points:

- the first step aims to measure the shape defects of the entire specimen at the unit cell scale. It is done with 35 RBF control points evenly distributed around the CAD model mesh with $r = 0.85 h$, as used previously in Section 4 (Figure 4)
- the second step aims to measure with more precision the shape defects around the upper vertex of the specimen so that the local beam shape and printing defects can be detected. The shape defects are now measured by 165 RBF control points distributed uniformly around the upper vertex with $r = 1.2 h$ (Figure 10).

The computational time is roughly proportional to the number of RBF control points, making the second step around 5 times more expensive.

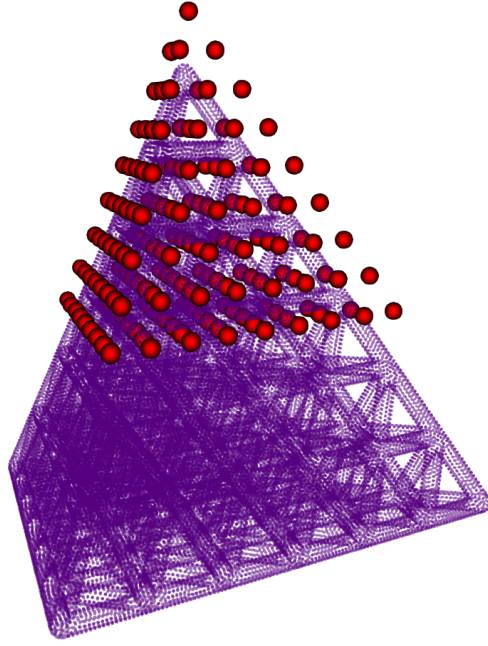


Fig. 10: Initial location of the 165 RBF control points (red) for the second step.

The exact shape of the specimen being unknown, the measurement error Δ as defined by Equation 19 is no more available. However, as usual in both VIC and DIC, we use the registration error maps defined as:

$$\delta_{\theta} = |F_{\theta} - G_{\theta}|. \quad (20)$$

Figure 11 shows the decrease of one of them during the whole process:

- The map after manual setting (a) show large registration error. It enables minimization to be started.
- The map after the calibration step (b) puts in good coincidence the virtual and real projections. Only the small defects from the prescribed CAD shape appear with light colors.

- After the 35 RBF control point step, the error map (c) is quite everywhere lower than 0.1.
- After the 165 RBF control points step (d), the error is close to 0 around the top vertex.

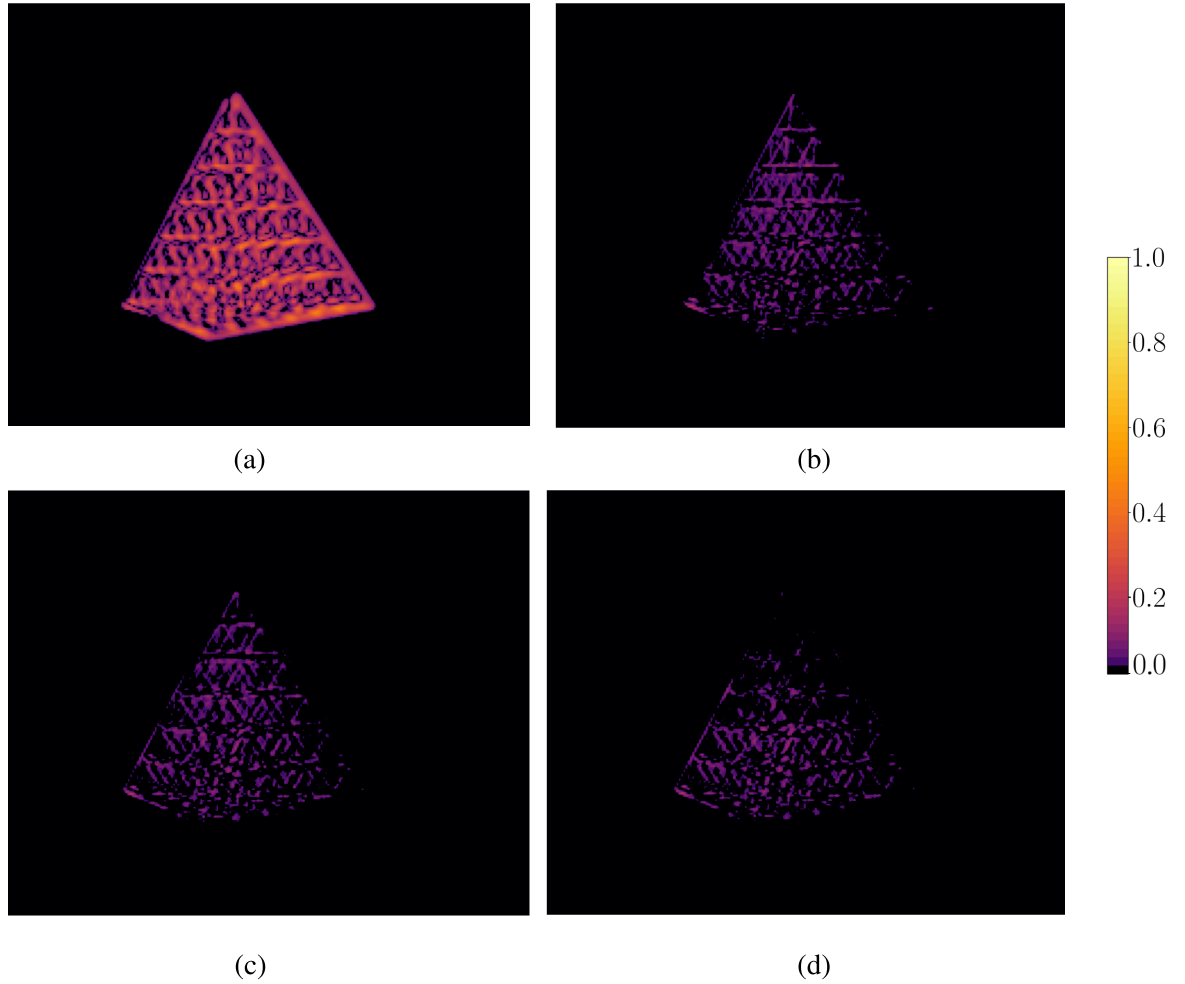


Fig. 11: Error maps δ_θ for $\theta = 63^\circ$ after (a) manual setup, (b) calibration, (c) 35 RBF control points measurement, (d) 165 RBF control points around the upper vertex measurement.

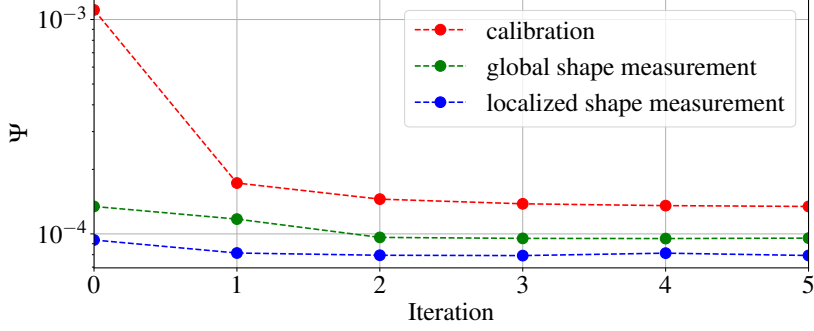


Fig. 12: Evolution of the cost function Ψ during the iterative registration process.

The convergence of the method is also visible on the convergence chart (Figure 12). It starts at $\Psi = 1.109 \times 10^{-3}$ and decreases to $\Psi = 7.900 \times 10^{-5}$. The quick convergence in less than 6 iterations, already observed in the synthetic tests of the previous Section 4, is confirmed in this real test. The gain during the local measure is due to the presence of shape defects in this region (Figure 13). In the future, it is therefore conceivable to strategically place control nodes in areas where the error map has large values, in order to perform a more local shape measurement there.

Figure 13 represents the final result of the 3D-VIC measure. The visible shape defects are at the cell scale, not at the pixel, CAD nodes or RBF grid scales, suggesting that they are not some artefacts. At the last step, the 165 RBF control points grid is fine enough to catch the beam diameter variation and beam curvature. Let us recall that the pixel size in the projections is close to the quarter of the beam diameter.

Some unexpected measured defects, not visible to the naked eye on the CTscan in Figure 8, can be explained by the manufacturing process. For example, Figure 14 shows, for some beams close to the top of the upper vertex, misalignment defects in the middle of some bars. We can see that these defects were caused by imperfect printing trajectories, which lead to stops and restarts in the printing path. We also observe that bars produced in a single trajectory do not show these localized defects, but only

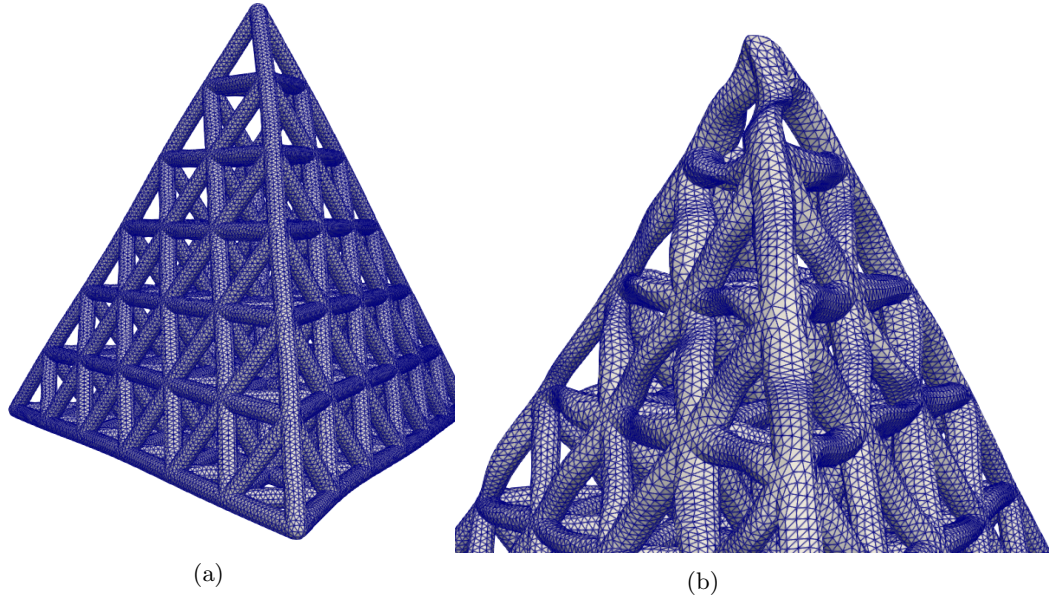


Fig. 13: (a) $\times 10$ magnified displacement from the initial CAD model after the global 35 RBF points measure. (b) $\times 2.5$ magnified displacement from the initial CAD model after the local 165 RBF points measure.

a curvature possibly due to local buckling or gravitational effect during printing. The pixel size visible in this figure shows that 3D-VIC can be used to measure fine defects without the need for very high image resolution.

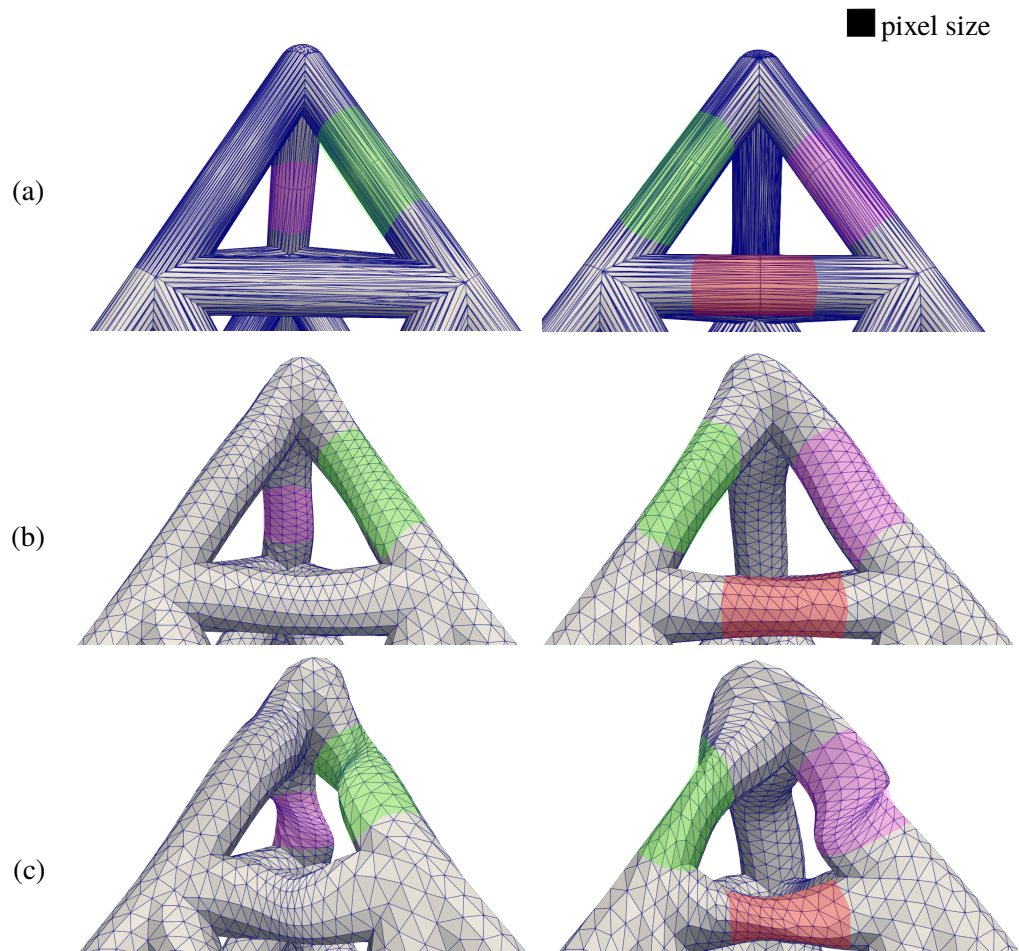


Fig. 14: Upper vertex detail. (a) mesh used for printing. 3D printing connection areas are colored. (b) true scale displacement from the initial CAD model after the global 35 RBF points measure (c) $\times 2.5$ magnified displacement from the initial CAD model after the local 165 RBF points measure

6 Discussion and conclusions

The presented 3D-VIC shape measurement method is an extension the Virtual Image Correlation (VIC) technique into three dimensions. Contrary to previous developments ([11, 12, 22]), it does not use at all the classical reconstructed 3D image of X-ray computed tomography, but only the 2D projections. This allows the use of a very limited set of projections, instead of some thousands in classical tomography. This has been made possible by the use of an efficient Z-buffer method for the thickness computations and the use of a well defined RBF method for the basis of displacements. The method has been shown to be able to measure the shape defects at sub-pixel scale.

As presented, the method was made under simplifying assumptions, as a perfect tomograph geometry, a punctual X-ray source and in absence of diffusion or scattering. Adding other tomograph parameters in the calibration phase is straightforward in the proposed framework. Following Fragnaud [11], it will be possible to take into account scattering and diffusion. However, if these defects are exacerbated by 3D image reconstruction processes, this is not the case with the proposed 3D-VIC method in which only projections are considered. For example, a bad pixel in the sensor may have a weak effect with the presented method using projections but, often leading to a well-known ring artefact in 3D reconstructed images, it may deeply affect methods using them. Furthermore, the result in Figure 7 and previous studies for the 2D VIC [21] suggest that the 3D-VIC is relatively insensitive to moderate blurring effects. In the same spirit, if the printed material contains small voids or inclusions (compared to the truss diameter) then the projections exhibit low and local grey level variations which can be handled by the proposed method. In the case where the object is made of different homogenous materials whose spatial distribution can be related to the CAD model, then the tomograph model can be modified considering

two or more X-ray absorption coefficients when computing the virtual projections. This also comes as a possible extension of the proposed method.

The size of the lattice material specimen was here of 56 cells. Larger ones are possible until the projections are enough contrasted at the points where the rays intersect the largest number of beams, *i.e.* the center of the specimen. This limitation is not specific to the 3D-VIC method.

The number and the location of the control points of the Radial Basis Functions depend upon the researched kind of defects. This ranges from a few points for global shape defects to a lot of points in the location where are the localized defects. Setting directly a large number of control points may require a large computing time and may lead to some instability if the control points cross each other, resulting in a loss of the initial topology. The proposed process in two (or more) steps seems more adapted and could evolve towards an automatic refinement of the control points where the error maps show large correlation errors.

A future application will involve capturing tomographic projections of a lattice specimen during mechanical tests, enabling shape and displacement measurements using this algorithm throughout the test. This approach will provide us with a CAD model of the initial specimen before loading, as well as a deformed mesh after loading, with a precision better than the size of the projection pixels. This will allow the measurement of the equivalent homogeneous elastic tensor and of the linearity of linearity surface, and to compare them to the theoretical values as obtained by [8, 41]

Competing interests

The authors have no competing interests to declare that are relevant to the content of this article.

Funding

This research was funded, in whole or in part, by French Agence Nationale de la Recherche ANR-19-CE10-0005 within the MoMaP program. A CC-BY public copyright license has been applied by the authors to the present document and will be applied to all subsequent, versions up to the Author Accepted Manuscript arising from this submission, in accordance with the grant's open access conditions.

References

- [1] Fleck, N., Deshpande, V.S., Ashby, M.: Micro-architected materials: Past, present and future. *Proceedings of The Royal Society A: Mathematical, Physical and Engineering Sciences* **466**, 2495–2516 (2010) <https://doi.org/10.1098/rspa.2010.0215>
- [2] Kaur, I., Singh, P.: State-of-the-art in heat exchanger additive manufacturing. *International Journal of Heat and Mass Transfer* **178**, 121600 (2021) <https://doi.org/10.1016/j.ijheatmasstransfer.2021.121600>
- [3] Alsulami, M., Mortazavi, M., Niknam, S.A., Li, D.: Design complexity and performance analysis in additively manufactured heat exchangers. *The International Journal of Advanced Manufacturing Technology* **110**(3), 865–873 (2020) <https://doi.org/10.1007/s00170-020-05898-3>
- [4] Rosi, G., Auffray, N.: Anisotropic and dispersive wave propagation within strain-gradient framework. *Wave Motion* **63**, 120–134 (2016) <https://doi.org/10.1016/>

- [5] du Plessis, A., Razavi, N., Benedetti, M., Murchio, S., Leary, M., Watson, M., Bhate, D., Berto, F.: Properties and applications of additively manufactured metallic cellular materials: A review. *Progress in Materials Science* **125**, 100918 (2022) <https://doi.org/10.1016/j.pmatsci.2021.100918>
- [6] Brechet, Y., Embury, D.: Architected materials: Expanding materials space. *Scripta Materialia* **68**(1), 1–3 (2013) <https://doi.org/10.1016/j.scriptamat.2012.07.038> . Architected Materials
- [7] Estrin, Y., Beygelzimer, Y., Kulagin, R.: Design of architected materials based on mechanically-driven structural and compositional patterning. *Advanced Engineering Materials* **21** (2019) <https://doi.org/10.1002/adem.201900487>
- [8] Jeanneau, V., Combescure, C., François, M.L.M.: Homogenized elasticity and domain of linear elasticity of 2D architected materials. *International Journal of Solids and Structures* **269**, 112185 (2023) <https://doi.org/10.1016/j.ijsolstr.2023.112185>
- [9] Glacet, A., Tanguy, A., Réthoré, J.: Vibrational properties of quasi-periodic beam structures. *Journal of Sound and Vibration* **442**, 624–644 (2019) <https://doi.org/10.1016/j.jsv.2018.10.045> . Accessed 2023-09-12
- [10] Somera, A., Poncelet, M., Auffray, N., Réthoré, J.: Quasi-periodic lattices: Pattern matters too. *Scripta Materialia* **209**, 114378 (2022) <https://doi.org/10.1016/j.scriptamat.2021.114378> . Accessed 2023-09-12
- [11] Fragnaud, C., Remacha, C., Betancur, J., Roux, S.: CAD-based X-ray CT calibration and error compensation. *Measurement Science and Technology* **33**(6), 065024 (2022) <https://doi.org/10.1088/1361-6501/ac5133> . Accessed 2023-07-13

- [12] Pastre, M.-A., Quinsat, Y., Lartigue, C.: Shape defect analysis from volumetric data - Application to lattice struts in additive manufacturing. *Precision Engineering* **76**, 12–28 (2022) <https://doi.org/10.1016/j.precisioneng.2022.02.011> . Accessed 2023-07-13
- [13] Sutton, M.A., McNeill, S.R., Helm, J.D., Chao, Y.J.: Advances in two-dimensional and three-dimensional computer vision. (2000)
- [14] Sutton, M., McNeill, S., Helm, J., Schreier, H.: Computer vision applied to shape and deformation measurement, pp. 571–632 (2000). <https://doi.org/10.1016/B978-008043020-1/50039-9>
- [15] Garcia, D., Orteu, J.J., Penazzi, L.: A combined temporal tracking and stereo-correlation technique for accurate measurement of 3D displacements: application to sheet metal forming. *Journal of Materials Processing Technology* **125-126**, 736–742 (2002) [https://doi.org/10.1016/S0924-0136\(02\)00380-1](https://doi.org/10.1016/S0924-0136(02)00380-1)
- [16] Luo, P.F., Chao, Y.J., Sutton, M.A., Peters, W.H.: Accurate measurement of three-dimensional deformations in deformable and rigid bodies using computer vision. *Experimental Mechanics* **33**(2), 123–132 (1993) <https://doi.org/10.1007/BF02322488>
- [17] Cardenas-Garcia, J.F., Yao, H.G., Zheng, S.: 3D reconstruction of objects using stereo imaging. *Optics and Lasers in Engineering* **22**(3), 193–213 (1995) [https://doi.org/10.1016/0143-8166\(94\)00046-D](https://doi.org/10.1016/0143-8166(94)00046-D) . *Computer Aided Measurement and Inspection*
- [18] Fouque, R., Bouclier, R., Passieux, J.-C., Périé, J.-N.: Photometric DIC: a unified framework for global Stereo Digital Image Correlation based on the construction of textured digital twins. *Journal of Theoretical, Computational and Applied*

Mechanics (2022) <https://doi.org/10.46298/jtcam.7467>

- [19] Semin, B., Auradou, H., François, M.: Accurate measurement of curvilinear shapes by Virtual Image Correlation. *European Physical Journal: Applied Physics* **56**(1), 10701 (2011) <https://doi.org/10.1051/epjap/2011110275> . Publisher: EDP Sciences. Accessed 2022-03-10
- [20] Réthoré, J., François, M.: Curve and boundaries measurement using B-splines and virtual images. *Optics and Lasers in Engineering* **52**, 145–155 (2013) <https://doi.org/10.1016/j.optlaseng.2013.06.018> . Publisher: Elsevier. Accessed 2022-03-10
- [21] François, M.L.M.: Uncertainty of the virtual image correlation method. *International Journal for Numerical Methods in Engineering* **123**(18), 4367–4390 (2022) <https://doi.org/10.1002/nme.7037>
- [22] Jiang, Z., Witz, J., Lecomte-Grosbras, P., Dequidt, J., Duriez, C., Cosson, M., Cotin, S., Brieu, M.: B-spline based multi-organ detection in magnetic resonance imaging. *Strain* **247**, 51–235 (2015)
- [23] Bay, B.K., Smith, T.S., Fyhrie, D.P., Saad, M.: Digital volume correlation: Three-dimensional strain mapping using X-ray tomography. *Experimental Mechanics* **39**(3), 217–226 (1999) <https://doi.org/10.1007/BF02323555>
- [24] Benoit, A., Guérard, S., Gillet, B., Guillot, G., Hild, F., Mitton, D., Périé, J.-N., Roux, S.: 3D analysis from micro-MRI during in situ compression on cancellous bone. *Journal of Biomechanics* **42**(14), 2381–2386 (2009) <https://doi.org/10.1016/j.jbiomech.2009.06.034>
- [25] Leclerc, H., Roux, S., Hild, F.: Projection Savings in CT-based Digital Volume Correlation. *Experimental Mechanics* **55**(1), 275–287 (2015) <https://doi.org/10.1007/s11340-014-9871-5>

- [26] Jailin, C.: Projection-based in-situ 4D mechanical testing. Theses, Université Paris Saclay (COMUE) (September 2018). <https://theses.hal.science/tel-01927948>
- [27] Lachambre, J., Réthoré, J., Weck, A., Buffiere, J.-Y.: Extraction of stress intensity factors for 3D small fatigue cracks using digital volume correlation and X-ray tomography. *International Journal of Fatigue* **71**, 3–10 (2015)
- [28] Buhmann, M.D.: *Radial Basis Functions: Theory and Implementations*. Cambridge Monographs on Applied and Computational Mathematics. Cambridge University Press, (2003). <https://doi.org/10.1017/CBO9780511543241>
- [29] Koo, J., Dahl, A.B., Bærentzen, J.A., Chen, Q., Bals, S., Dahl, V.A.: Shape from Projections via Differentiable Forward Projector for Computed Tomography. *Ultramicroscopy* **224**, 113239 (2021) <https://doi.org/10.1016/j.ultramic.2021.113239> . arXiv: 2006.16120. Accessed 2022-04-11
- [30] Davidovič, T., Engelhardt, T., Georgiev, I., Slusallek, P., Dachsbacher, C.: 3D rasterization: A bridge between rasterization and ray casting, pp. 201–208 (2012)
- [31] Marschner, S., Shirley, P.: *Fundamentals of Computer Graphics vol. 2,3,4*. CRC Press, (2018)
- [32] Friedrichsdorf, S.P., Arana-Chavez, V.E., Cattaneo, P.M., Spin-Neto, R., Dominguez, G.C.: Effect of the software binning and averaging data during micro-computed tomography image acquisition. *Scientific Reports* **9**(1), 10562 (2019) <https://doi.org/10.1038/s41598-019-46530-z> . Number: 1 Publisher: Nature Publishing Group. Accessed 2023-10-12
- [33] Baek, J., Pineda, A.R., Pelc, N.J.: To bin or not to bin? The effect of CT system limiting resolution on noise and detectability. *Physics in Medicine and*

- Biology **58**(5), 1433–1446 (2013) <https://doi.org/10.1088/0031-9155/58/5/1433>
. Accessed 2023-07-14
- [34] Hild, F., Roux, S.: Comparison of Local and Global Approaches to Digital Image Correlation. *Experimental Mechanics* **52**(9), 1503–1519 (2012) <https://doi.org/10.1007/s11340-012-9603-7> . Accessed 2023-09-12
- [35] Passieux, J., Bouclier, R.: Classic and inverse compositional Gauss-Newton in global DIC. *International Journal for Numerical Methods in Engineering* **119**(6), 453–468 (2019) <https://doi.org/10.1002/nme.6057> . Accessed 2023-09-12
- [36] Sutton, M.A., Ortu, J.-J., Schreier, H.W.: *Image Correlation for Shape, Motion and Deformation Measurements : Basic Concepts, Theory and Applications*, p. 321. Springer, (2009). <https://doi.org/10.1007/978-0-387-78747-3> . <https://imt-mines-albi.hal.science/hal-01729219>
- [37] Henneron, T., Pierquin, A., Clénet, S.: Mesh Deformation Based on Radial Basis Function Interpolation Applied to Low-Frequency Electromagnetic Problem. *IEEE Transactions on Magnetics* **14**, 1–4 (2019) <https://doi.org/10.1109/TMAG.2019.2896623>
- [38] Botsch, M., Kobbelt, L.P.: Real-time shape editing using Radial Basis Functions. *Computer Graphics Forum* **24** (2005)
- [39] Tezzele, M., Demo, N., Mola, A., Rozza, G.: PyGeM: Python Geometrical Morphing. *Software Impacts* **7**, 100047 (2021) <https://doi.org/10.1016/j.simpa.2020.100047> . Accessed 2022-04-06
- [40] Dawson-Haggerty et al.: Trimesh. <https://trimesh.org/>
- [41] François, M.L.M., Chen, L., Coret, M.: Elasticity and symmetry of triangular

lattice materials. *International Journal of Solids and Structures* **129**, 18–27 (2017)

<https://doi.org/10.1016/j.ijsolstr.2017.09.019>